What Drives the Variability of Evaporative Demand across the Conterminous United States?

MICHAEL HOBBINS AND ANDREW WOOD*

NOAA/NWS/Colorado Basin River Forecast Center, Salt Lake City, Utah

DAVID STREUBEL

NOAA/NWS/Alaska-Pacific River Forecast Center, Anchorage, Alaska

KEVIN WERNER

NOAA/NWS/Colorado Basin River Forecast Center, Salt Lake City, Utah

(Manuscript received 18 August 2011, in final form 10 April 2012)

ABSTRACT

To understand the sources of temporal and spatial variability of atmospheric evaporative demand across the conterminous United States (CONUS), a mean-value, second-moment uncertainty analysis is applied to a spatially distributed dataset of daily synthetic pan evaporation for 1980–2009. This evaporative demand measure is from the ''PenPan'' model, which is a combination equation calibrated to mimic observations from U.S. class-A evaporation pans and here driven by six North American Land Data Assimilation System variables: temperature, specific humidity, station pressure, wind speed, and downwelling shortwave and longwave radiation. The variability of evaporative demand is decomposed across various time scales into contributions from these drivers. Contrary to popular expectation and much hydrologic practice, temperature is not always the most significant driver of temporal variability in evaporative demand, particularly at subannual time scales. Instead, depending on the season, one of four drivers (temperature, specific humidity, downwelling shortwave radiation, and wind speed) dominates across different regions of CONUS. Temperature generally dominates in the northern continental interior. This analysis assists land surface modelers in balancing parameter parsimony and physical representativeness. Patterns of dominant drivers are shown to cycle seasonally, with clear implications for modeling evaporative demand in operational hydrology or as a metric of climate change and variability. Depending on the region and season, temperature, specific humidity, downwelling shortwave radiation, and wind speed must together be examined, with downwelling longwave radiation as a secondary input. If any variable may be ignored, it is atmospheric pressure. Parameterizations of evaporative demand based solely on temperature should be avoided at all time scales.

1. Introduction

The distribution of soil and vegetative moisture is essentially unknowable at temporal and spatial scales useful to water managers. Instead, hydrologists interested in quantifying the moisture flux from the terrestrial surface to the atmosphere—that is, actual evapotranspiration (ET)—use the concept of atmospheric evaporative demand (E_0) to quantify ET's upper limit. ET is then estimated by scaling down from E_0 using simple vegetation-related coefficients or land surface models (LSMs) that account for actual (unknown) moisture conditions and/or vegetative moisture transfer. This paradigm underpins much of operational hydrology, including streamflow prediction, water management in both municipalities and agriculture, and other decision-making enterprises that rely on real-time quantification of surface water availability. This widespread use of E_0 motivates a need for operationally and scientifically sound E_0 measures—measures that rely on physically appropriate forcings,

* Current affiliation: NOAA/NWS/Northwest River Forecast Center, Portland, Oregon.

Corresponding author address: Michael Hobbins, NOAA/NWS/Colorado Basin River Forecast Center, 2242 W North Temple, Salt Lake City, UT 84116.
E-mail: mike.hobbins@noaa.gov

FIG. 1. A typical U.S. class-A evaporation pan. (Photo courtesy of the U.S. National Weather Service.)

that yield accurate results at time and space scales relevant to operational goals, and that avoid extraneous modeling uncertainty or the omission of key sources of variability. Understanding the drivers of space and time variability of physically based E_0 underpinning our modeling approaches is a valuable step toward meeting this need.

Traditional measures of E_0 range from simple temperature-based empirical models (e.g., Thornthwaite 1948; Blaney and Criddle 1950; Hamon 1961; Hargreaves and Samani 1985) to more complex, physically based parameterizations of the radiative and advective dynamics at the land surface–atmosphere interface. The latter formulations are usually based on the combination equation of Penman (1948). Observation-based E_0 measures—most commonly the U.S. class-A evaporation pan (see Fig. 1)—are affordable and simple, leading to their long-term, worldwide use in agricultural settings (Stanhill 2002) and, recently, as a metric of long-term hydroclimatologic change and variability (Peterson et al. 1995; Brutsaert and Parlange 1998; Ohmura and Wild 2002; Roderick and Farquhar 2002; Hobbins et al. 2004, 2008; Roderick et al. 2009a,b). However, despite the physical representativeness of pan evaporation (E_{pan}) observations, hydrologic operations such as streamflow forecasting and water management require spatially continuous estimates in the past and the future. Frequently these hydrologic operations use the simplistic temperature-based E_0 approaches that distill E_0 variability down to that of a single driver (temperature). This reliance on simplistic representations of E_0 also extends to drought monitoring and to climate research on longer time scales: for example, in the Palmer drought severity index (PDSI; Palmer 1965), which is central to much of

current drought-monitoring practice in the United States (e.g., in the U.S. Drought Monitor of Svoboda et al. 2002) and to worldwide, long-term drought-trend analyses (e.g., Dai et al. 2004). Reliance on ET from the PDSI's E_0-forced surface hydrology model (see supporting information in Hobbins et al. 2008 for details) has led to indications of drying under warming that have been shown to be contrary to both observations and model results forced by E_0 observations from evaporation pans (Moonen et al. 2002; Chen et al. 2005; Hobbins et al. 2008). In this context, the benefits of using a more physically representative calculation across all time scales and a more realistic E_0 are clear.

Simple sensitivity analyses can quantify the degree to which a hydrologic variable responds to its hydrometeorologic drivers, but do not account for the observed variability of those drivers. For example, Eslamian et al.'s (2011) finding that Penman–Monteith reference ET is extremely sensitive to variations in relative humidity is useful insofar as we establish that relative humidity is, in fact, variable at all. If a driver is nearly constant, the sensitivity of the response variable to it is moot. Robust examination of long-term trends and variability in the hydrologic cycle must address the central questions, ''What meteorological and/or radiative input(s) drive the spatial and temporal variability of E_0? And do our chosen methods capture this variability?'' Answering these questions is the primary motivation of this paper.

In this study, we use a physically based formulation of E_0—the so-called PenPan model of Rotstayn et al. (2006), which is a Penman-based equation that replicates E_{pan} observations well—to synthesize conterminous United States (CONUS)-wide surfaces of E_{pan}. This model is outlined in section 2 and appendix A. In our examination of the temporal and spatial variability of modeled E_0 across various time scales, we move beyond a pure sensitivity analysis; instead, we enhance our knowledge of sensitivities of E_0 to its drivers by applying a mean-value second-order uncertainty protocol (Mailhot and Villeneuve 2003). We first analytically derive the sensitivities of the response variable (in our case, E_{pan}) to its drivers (e.g., temperature). To these sensitivities, we then apply the observed variability of each driver varying alone and in pairs, thereby permitting a decomposition of the temporal variability of E_{pan} across space into the relative contributions from all of its drivers. In general, such an analysis will identify which drivers— by dint of their own uncertainty or variability—may introduce the greatest error, and thus may require the most correction effort, and which drivers are essential to achieve both model parameter parsimony and physical representation.

2. Methodology

Sections 2a and 2b briefly describe the PenPan model and the forcing datasets used and summarize the resulting E_{pan} reanalysis used for E_0 used in the variability analysis. Section 2c compares the new E_{pan} reanalysis to observed monthly E_{pan} observations and to an atlas of E_{pan} climatology. Section 2d describes the concept of the variability analysis. In section 2e, the spatial distributions of the sensitivities of the E_{pan} model to its drivers are summarized (the sensitivity expressions are derived in appendix A). Section 2f describes the metric for quantifying contributions to E_{pan} variability by each of its drivers.

a. E_{pan} formulation and data

In his seminal work, Penman (1948) codified the concept of atmospheric evaporative demand in a "combination equation" for potential evaporation, and verified it against E_{pan} observations. The Penman equation is the core of most physically based models of E_0—that is, models that account for both advective and radiative forcings—including the "PenPan" model used in this study. Essentially, the PenPan model is a Penman equation adjusted such that standard meteorological data and further climate model data can drive simulations of U.S. class-A pan evaporation (Fig. 1; details in appendix Aa). The model arose from work on the radiative (Linacre 1994) and advective (Thom et al. 1981) drivers of E_{pan} that together resolve the differences between Penman's (1948) potential evaporation for a flat surface and that for the above-ground U.S. class-A evaporation pan. In the PenPan model, Rotstayn et al. (2006) combined these enhancements of driver characterizations to account for the extra solar radiation intercepted by pan walls, the extra surface area for sensible heat transfer, and the effects of turbulence over the water surface resulting from the pan walls. It is becoming a widely used E_{pan} model, and has been driven by both observations and climate model data to decompose past monthly E_{pan} trends (Roderick et al. 2007), to verify GCM outputs (Rotstayn et al. 2006), to examine E_{pan} trends as estimated by reanalyses products and predicted by GCMs (Johnson and Sharma 2010), and to examine land surface–atmosphere interactions that result in changes in both point E_0 and areal ET (Shuttleworth et al. 2009). PenPan-derived E_{pan} has been shown to closely match observations of monthly E_{pan} across Australia (Roderick et al. 2007); the results of a similar verification across CONUS are described in section 2c. The PenPan formulation—shown in more detail in appendix Aa—is summarized here:

$$E_{pan} = \frac{\Delta}{\Delta + a_p \gamma} \frac{Q_n}{\lambda} + \frac{a_p \gamma}{\Delta + a_p \gamma} f_q(U_2)(e_{sat} - e_a), \quad (1)$$

where E_{pan} is in kg m^{-2} s^{-1} (equivalent to mm s^{-1}); Q_n is the net available energy [W m^{-2}; Eq. (A8)]; $f_q(U_2)$ is a "wind function" [kg m^{-2} s^{-1} Pa^{-1}; Eq. (A9)] of the 2-m wind speed U_2 (m s^{-1}); e_{sat} and e_a are the saturated and actual vapor pressures (Pa), respectively [Eqs. (A11) and (A12)]; λ is the latent heat of vaporization [J kg^{-1}; Eq. (A13)]; Δ is de_{sat}/dT (Pa K^{-1}) at T (K); a_P is the ratio of effective surface areas for heat and water-vapor transfer in a pan [Eq. (A10)]; and γ is the psychrometric constant (Pa K^{-1}). To obtain E_{pan} in the more familiar units of mm day^{-1}, multiply by 86 400.

b. 30-yr reanalysis of E_{pan}

We used the PenPan formulation to generate a 30-yr, daily reanalysis of E_{pan} across CONUS at a 0.125° resolution from 1 January 1980 to 31 December 2009. The model is driven only by the following six meteorological and radiation drivers drawn from the North American Land Data Assimilation System (NLDAS; Mitchell et al. 2004): 2-m air temperature T (K), 2-m specific humidity q (kg kg^{-1}), surface pressure P_{atm} (Pa), zonal and meridional components of 10-m wind speed U_{10} (m s^{-1}), downwelling shortwave radiation R_d (W m^{-2}), and downwelling longwave radiation L_d (W m^{-2}). The 2-m wind speed U_2 (m s^{-1}) required for the PenPan model is scaled from U_{10} assuming the following vertical profile of wind speed (Brutsaert 1982):

$$U_{z_1} = U_{z_2} \left(\frac{z_1}{z_2}\right)^{1/7}, \quad (2)$$

where U_z is the wind speed at height z (m) above the ground and z_1 and z_2 are the heights at which wind speeds are required and available (10 m here), respectively. For application in the model, the hourly reanalysis drivers are aggregated to daily means (the wind components are first converted to hourly wind speeds). In the framework of a variability analysis, these drivers are specified as random variables normally distributed with a known mean and variance.

Figure 2 summarizes the mean annual E_{pan} and the standard deviations of annual, January, and July E_{pan} aggregated from daily totals; similar results may be obtained for time scales as short as individual days. In line with (but independent of) observations from evaporation pans, our synthetic annual E_{pan} is highest in the sunniest, warmest, driest, and windiest regions of CONUS (Fig. 2a). The annual variability of E_{pan}—here estimated by its standard deviation—does not match the spatial pattern of its annual magnitude. The greatest variability lies in a swath covering the Texas and Gulf Coast region and the High Plains, with a further regional maximum in
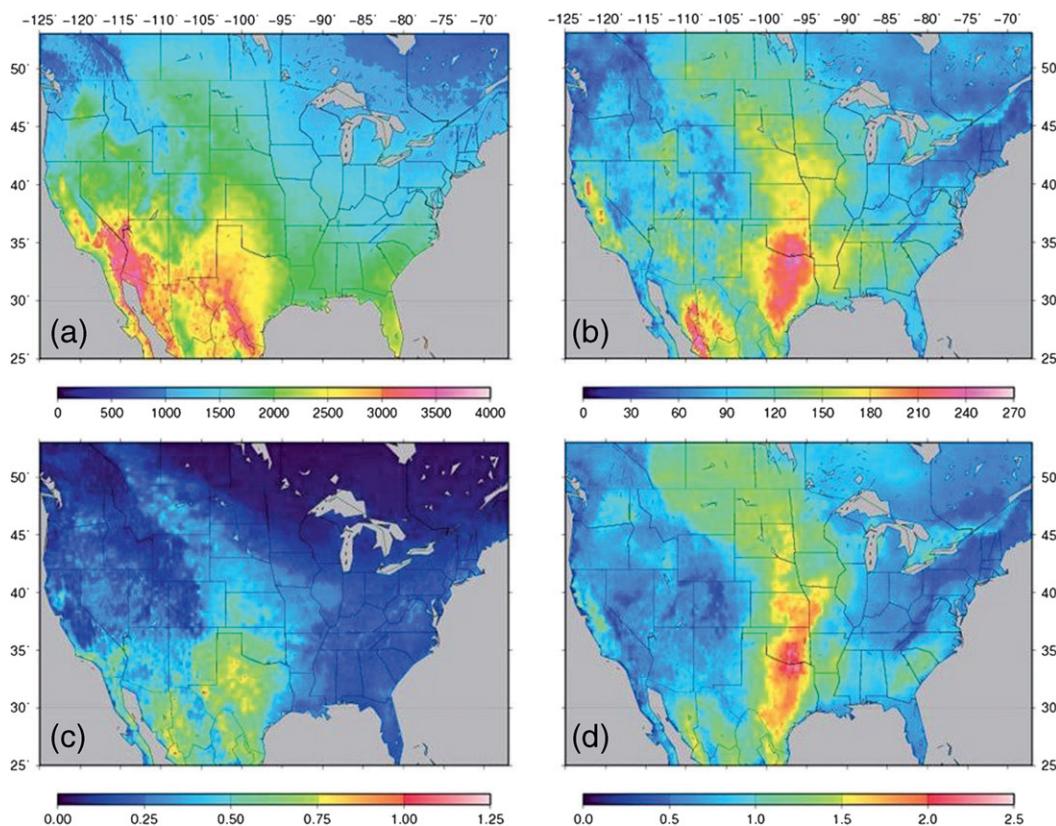
FIG. 2. The spatial variability of E_{pan}, as estimated by the PenPan model driven by NLDAS data for 1980–2009: (a) mean annual E_{pan} (mm yr^{-1}), and standard deviations of (b) annual E_{pan} (mm yr^{-1}), (c) January E_{pan} (mm month^{-1}), and (d) July E_{pan} (mm month^{-1}).

Northern and central California (Fig. 2b). To demonstrate the intra-annual change of variability in E_{pan}, we contrast January (Fig. 2c), when the area of greatest variability is in Texas and eastern New Mexico, with July (Fig. 2d), when the greatest variability is found in the U.S. High Plains (and the prairies of Canada), with a maximum in northern Texas, Oklahoma, and Kansas.

c. Verification of NLDAS-driven, PenPan-derived E_{pan} across CONUS

We verify our NLDAS-driven, PenPan-modeled E_{pan} estimate of E_0 against observations across CONUS: first in spatial distribution, then in the mean, and finally in the variability.

To verify the spatial distribution, we compared our climatological warm-season [i.e., May–October (MJJASO)] E_{pan} surface to the widely used version of the same in the Farnsworth et al. (1982) atlas (map 1; as this latter map is not available in a useful digital format, this comparison is not shown here). However, various caveats apply to the comparison. First, the Farnsworth et al. (1982) map is not simply interpolated climatological mean

warm-season E_{pan}: the source data are drawn from various pan types—class-A pans, sunken pans, and floating pans—and from E_{pan} estimated using the Penman (1948) equation. Second, across western CONUS and mountainous areas of eastern CONUS, Farnsworth et al. (1982) correct their E_{pan} estimates for elevation within physiographic regions. Third, their E_{pan}-elevation relations are estimated by eye and their final map is drawn by hand. Finally, the time periods do not coincide: in this study we use 1980–2009, whereas Farnsworth et al. (1982) use 1956–70. Caveats notwithstanding, the broad spatial patterns and features of both surfaces match well: regional troughs and ridges coincide; both represent well the topographic heterogeneity of western CONUS and the Appalachian region of eastern CONUS; both show E_{pan} declining with latitude in eastern CONUS and with elevation CONUS-wide; and both show higher E_{pan} in sunnier, windier, warmer, and drier regions, with maxima in the lower valleys of the desert Southwest.

The means and variabilities of our modeled E_{pan} are verified against observed E_{pan} from 251 evaporation pans in the National Climatic Data Center (NCDC) Summary
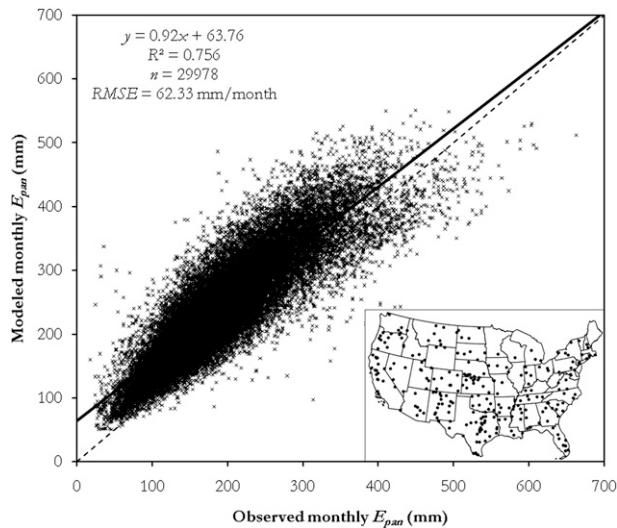
FIG. 3. Verification of the NLDAS-driven, PenPan-modeled E_{pan} against observed E_{pan} drawn from the class-A evaporation pans across CONUS for the warm season (i.e., MJJASO). Verification data are 29 978 monthly E_{pan} totals from 251 pans shown in the inset map. The dashed line represents a perfect fit. The solid line represents the best fit of the modeled E_{pan} to this lumped population; the statistics of the fits to individual months are shown in Table 1.

of the Day (NCDC 2011a) and NCDC Summary of the Month (NCDC 2011b) datasets. Observations of E_{pan} are drawn from those pans reporting >66% of warm-season months (i.e., >95 months) in the period May 1979 to August 2002. This verification dataset maximizes geographic coverage of the fit while capturing the growing season across the vast majority of CONUS (a CONUS-wide, year-round verification is not possible because of the freezing of pans across most of the domain).

The fit of our modeled E_{pan} to observed CONUS pan data is shown in Fig. 3. The primary reasons for the greater error here than in the Australian verification of

PenPan E_{pan} (Roderick et al. 2007) (see Table 1, bottom row) are our use of coarse (0.125°) gridded drivers as opposed to the site-specific point observations used in the Australian study, and that CONUS is more complex in topography and hydroclimate than Australia. Given that model calibrations are biased toward mean conditions and low-resolution reanalyses inputs are biased toward spatial mean conditions, one should expect poorer modeling of E_{pan} at the extremes and an underestimation of observed E_{pan} variability. This expectation is confirmed in the positive intercepts and subunity monthly slopes shown in Table 1, and in a direct comparison of variabilities, wherein we note that our modeling slightly underestimates observed variability, but that the variabilities correspond more closely in eastern CONUS and at less variable pans. Notwithstanding these caveats, this verification supports that of Roderick et al. (2007) in Australia. We conclude that, across CONUS, E_{pan} from the PenPan model corresponds well to observations of E_{pan} and of E_0 in general.

d. Variability analysis

We perform a mean-value, second-moment variability analysis (Mailhot and Villeneuve 2003) to decompose the variability observed in our synthetic E_{pan} into the contributions to variability that derive from all model drivers. In this section, we first outline the approach, in which we derive a general expression for E_{pan} variability expressed as contributions from the variabilities of, and sensitivity to, all of its drivers acting alone and covarying in all possible pairs [Eq. (7)]. In subsequent sections, we apply two simplifications to the model and derive analytic expressions of the sensitivities of E_{pan} to its drivers [Eqs. (A15)–(A20) in appendix Ab] and map the sensitivities to each driver, each driver's variance, and examples of covariances of drivers acting in pairs.

TABLE 1. The statistics of the monthly relations between observed and NLDAS-modeled E_{pan} across CONUS. The column marked "n (No. pans)" reports the number of monthly data drawn from the number of pans shown in the parentheses. The row marked "MJJASO lumped" is for the fit shown in Fig. 3. The bottom row summarizes the Australian verification described in Roderick et al. (2007) for comparison.

	n (No. pans)	R^2	RMSE (mm month^{-1})	Slope	Intercept (mm month^{-1})
May	5010 (251)	0.686	55.08	0.82	75.80
June	5275 (251)	0.711	65.57	0.80	95.82
July	5337 (251)	0.677	77.33	0.80	112.65
August	5281 (251)	0.666	70.78	0.78	105.01
September	5098 (251)	0.645	53.27	0.75	81.83
October	3977 (238)	0.598	38.08	0.68	63.58
MJJASO lumped	29 978 (251)	0.756	62.33	0.92	63.76
Australia, 12 months (Roderick et al. 2007)	5071 (26)	0.95	24	1.01	7.7

The strict derivation of the variability in our synthetic E_{pan} makes no assumptions about stationarity and uses only the six drivers as they are presented by NLDAS:

$$E_{pan} = f(T, q, P_{atm}, U_{10}, R_d, L_d). \tag{3}$$

In limiting our analysis to a second-order expansion, the variability in E_{pan} ($\sigma^2_{E_{pan}}$) derives from the variabilities in all of its drivers acting independently and covarying. These variability contributions require analytic expressions of the sensitivities of E_{pan} to each driver, the observed variance of each driver, and the observed covariance of each pair of drivers. The variability in E_{pan} may be expressed more concisely in matrix algebra form as

$$\sigma^2_{E_{pan}} \approx \boldsymbol{\gamma}^T \mathbf{C} \boldsymbol{\gamma}, \tag{4}$$

where $\boldsymbol{\gamma}$ is the vector of all drivers' sensitivities to E_{pan}, and $\boldsymbol{\gamma}^T$ its transpose, defined as

$$\boldsymbol{\gamma}^T \equiv \left[\frac{\partial E_{pan}}{\partial T} \quad \frac{\partial E_{pan}}{\partial q} \quad \frac{\partial E_{pan}}{\partial P_{atm}} \quad \frac{\partial E_{pan}}{\partial U_{10}} \quad \frac{\partial E_{pan}}{\partial R_d} \quad \frac{\partial E_{pan}}{\partial L_d} \right], \tag{5}$$

in which the partial derivatives (the sensitivity expressions) are analytic expressions evaluated at the drivers' means for each point in space; and $\mathbf{C}$ is the covariance matrix—that is, a matrix describing the variances σ^2_X of each driver and the covariances $\sigma_{X,Y}$ between each pair of drivers:

$$\mathbf{C} \equiv \begin{bmatrix} \sigma^2_T & \sigma_{T,q} & \sigma_{T,P_{atm}} & \sigma_{T,U_{10}} & \sigma_{T,R_d} & \sigma_{T,L_d} \\ \sigma_{q,T} & \sigma^2_q & \sigma_{q,P_{atm}} & \sigma_{q,U_{10}} & \sigma_{q,R_d} & \sigma_{q,L_d} \\ \sigma_{P_{atm},T} & \sigma_{P_{atm},q} & \sigma^2_{P_{atm}} & \sigma_{P_{atm},U_{10}} & \sigma_{P_{atm},R_d} & \sigma_{P_{atm},L_d} \\ \sigma_{U_{10},T} & \sigma_{U_{10},q} & \sigma_{U_{10},P_{atm}} & \sigma^2_{U_{10}} & \sigma_{U_{10},R_d} & \sigma_{U_{10},L_d} \\ \sigma_{R_d,T} & \sigma_{R_d,q} & \sigma_{R_d,P_{atm}} & \sigma_{R_d,U_{10}} & \sigma^2_{R_d} & \sigma_{R_d,L_d} \\ \sigma_{L_d,T} & \sigma_{L_d,q} & \sigma_{L_d,P_{atm}} & \sigma_{L_d,U_{10}} & \sigma_{L_d,R_d} & \sigma^2_{L_d} \end{bmatrix}. \tag{6}$$

Equation (4) for $\sigma^2_{E_{pan}}$ expands into the full expression of contributions from all of its drivers as follows:

$$\begin{aligned} \sigma^2_{E_{pan}} \approx & \frac{\partial E^2_{pan}}{\partial T}\sigma^2_T + \frac{\partial E_{pan}}{\partial T}\frac{\partial E_{pan}}{\partial q}\sigma_{T,q} + \frac{\partial E_{pan}}{\partial T}\frac{\partial E_{pan}}{\partial P_{atm}}\sigma_{T,P_{atm}} + \frac{\partial E_{pan}}{\partial T}\frac{\partial E_{pan}}{\partial U_{10}}\sigma_{T,U_{10}} + \frac{\partial E_{pan}}{\partial T}\frac{\partial E_{pan}}{\partial R_d}\sigma_{T,R_d} + \frac{\partial E_{pan}}{\partial T}\frac{\partial E_{pan}}{\partial L_d}\sigma_{T,L_d} \\ & + \frac{\partial E^2_{pan}}{\partial q}\sigma^2_q + \frac{\partial E_{pan}}{\partial q}\frac{\partial E_{pan}}{\partial T}\sigma_{q,T} + \frac{\partial E_{pan}}{\partial q}\frac{\partial E_{pan}}{\partial P_{atm}}\sigma_{q,P_{atm}} + \frac{\partial E_{pan}}{\partial q}\frac{\partial E_{pan}}{\partial U_{10}}\sigma_{q,U_{10}} + \frac{\partial E_{pan}}{\partial q}\frac{\partial E_{pan}}{\partial R_d}\sigma_{q,R_d} + \frac{\partial E_{pan}}{\partial q}\frac{\partial E_{pan}}{\partial L_d}\sigma_{q,L_d} \\ & + \frac{\partial E^2_{pan}}{\partial P_{atm}}\sigma^2_{P_{atm}} + \frac{\partial E_{pan}}{\partial P_{atm}}\frac{\partial E_{pan}}{\partial T}\sigma_{P_{atm},T} + \frac{\partial E_{pan}}{\partial P_{atm}}\frac{\partial E_{pan}}{\partial q}\sigma_{P_{atm},q} + \frac{\partial E_{pan}}{\partial P_{atm}}\frac{\partial E_{pan}}{\partial U_{10}}\sigma_{P_{atm},U_{10}} + \frac{\partial E_{pan}}{\partial P_{atm}}\frac{\partial E_{pan}}{\partial R_d}\sigma_{P_{atm},R_d} + \frac{\partial E_{pan}}{\partial P_{atm}}\frac{\partial E_{pan}}{\partial L_d}\sigma_{P_{atm},L_d} \\ & + \frac{\partial E^2_{pan}}{\partial U_{10}}\sigma^2_{U_{10}} + \frac{\partial E_{pan}}{\partial U_{10}}\frac{\partial E_{pan}}{\partial T}\sigma_{U_{10},T} + \frac{\partial E_{pan}}{\partial U_{10}}\frac{\partial E_{pan}}{\partial q}\sigma_{U_{10},q} + \frac{\partial E_{pan}}{\partial U_{10}}\frac{\partial E_{pan}}{\partial P_{atm}}\sigma_{U_{10},P_{atm}} + \frac{\partial E_{pan}}{\partial U_{10}}\frac{\partial E_{pan}}{\partial R_d}\sigma_{U_{10},R_d} + \frac{\partial E_{pan}}{\partial U_{10}}\frac{\partial E_{pan}}{\partial L_d}\sigma_{U_{10},L_d} \\ & + \frac{\partial E^2_{pan}}{\partial R_d}\sigma^2_{R_d} + \frac{\partial E_{pan}}{\partial R_d}\frac{\partial E_{pan}}{\partial T}\sigma_{R_d,T} + \frac{\partial E_{pan}}{\partial R_d}\frac{\partial E_{pan}}{\partial q}\sigma_{R_d,q} + \frac{\partial E_{pan}}{\partial R_d}\frac{\partial E_{pan}}{\partial P_{atm}}\sigma_{R_d,P_{atm}} + \frac{\partial E_{pan}}{\partial R_d}\frac{\partial E_{pan}}{\partial U_{10}}\sigma_{R_d,U_{10}} + \frac{\partial E_{pan}}{\partial R_d}\frac{\partial E_{pan}}{\partial L_d}\sigma_{R_d,L_d} \\ & + \frac{\partial E^2_{pan}}{\partial L_d}\sigma^2_{L_d} + \frac{\partial E_{pan}}{\partial L_d}\frac{\partial E_{pan}}{\partial T}\sigma_{L_d,T} + \frac{\partial E_{pan}}{\partial L_d}\frac{\partial E_{pan}}{\partial q}\sigma_{L_d,q} + \frac{\partial E_{pan}}{\partial L_d}\frac{\partial E_{pan}}{\partial P_{atm}}\sigma_{L_d,P_{atm}} + \frac{\partial E_{pan}}{\partial L_d}\frac{\partial E_{pan}}{\partial U_{10}}\sigma_{L_d,U_{10}} + \frac{\partial E_{pan}}{\partial L_d}\frac{\partial E_{pan}}{\partial R_d}\sigma_{L_d,R_d}. \end{aligned} \tag{7}$$

In Eq. (7), we consider each line on the right-hand side to represent the contributions to the variability in E_{pan} due to the inclusion of a single driver in the E_{pan} parameterization: the first term on the line representing that from the driver considered varying independently of other drivers, and the next five terms representing that from the driver covarying with all other drivers. Note that covariances are commutative (i.e., $\sigma_{Y,X} = \sigma_{X,Y}$), so terms for the contribution of a given pair of covarying drivers occur twice in Eq. (7); in this analysis, however, it is our goal to conserve variability to as great a degree as possible, so we ascribe one each of the pair of identical terms to each of the drivers. Thus, we aggregate the contribution (B_X) to overall E_{pan} variability of any single driver X as the magnitude of the sum of all terms in each line of Eq. (7), as follows:

$$B_X \equiv \frac{\partial E_{\text{pan}}}{\partial X}\left[\frac{\partial E_{\text{pan}}}{\partial X}\sigma_X^2 + \sum_{i=1}^{m}\left(\frac{\partial E_{\text{pan}}}{\partial Y_i}\sigma_{X,Y_i}\right)\right]. \quad (8)$$

The overall variability in E_{pan} from all n drivers is then

$$\sigma_{E_{\text{pan}}}^2 \approx \sum_{x=1}^{n} B_X. \quad (9)$$

All variances σ_X^2 and covariances $\sigma_{X,Y}$ are derived from time series analysis of the 30-yr NLDAS reanalysis dataset. The sensitivities of E_{pan} to its drivers $\partial E_{\text{pan}}/\partial X$ are derived analytically from the model formulation [Eq. (1)] and shown in Eqs. (A15)–(A20) after making a simple approximation for the dependency of Δ and γ on T (see appendix B). All sensitivities are evaluated at the drivers' temporal mean values across the relevant time scale, and their expressions are shown in appendix Ab.

e. Sensitivity of PenPan model to its drivers

Derivation of the sensitivities of PenPan-derived E_{pan} to its drivers $\partial E_{\text{pan}}/\partial X$ necessitates developing an expression of the PenPan equation [Eq. (1)] in terms of constants and the six time-varying independent random variables (i.e., the drivers) from the NLDAS dataset. The development of this expression is shown in appendix Aa, and the derivations of the sensitivities of E_{pan} to each of its drivers are shown in appendix Ab.

The spatial variation in the sensitivity of annual E_{pan} to each driver is shown in Fig. 4. Maps are derived by applying Eqs. (A15)–(A20) at each grid cell with annual means of all drivers. The graininess in the spatial patterns of some of the sensitivities (i.e., $\partial E_{\text{pan}}/\partial T$, $\partial E_{\text{pan}}/\partial q$, and $\partial E_{\text{pan}}/\partial P_{\text{atm}}$) is likely due to the NLDAS data assimilation of U_{10}. The other sensitivities that not are functions of U_{10}—$\partial E_{\text{pan}}/\partial U_{10}$, $\partial E_{\text{pan}}/\partial R_d$, and $\partial E_{\text{pan}}/\partial L_d$—are not grainy.

Of the six drivers' annual sensitivities exhibited in Fig. 4, the most complex spatial patterns are those of $\partial E_{\text{pan}}/\partial T$, and $\partial E_{\text{pan}}/\partial q$, because of the variety of drivers that appear in their expressions [Eqs. (A18) and (A20)]. For $\partial E_{\text{pan}}/\partial T$, a function of all six drivers [Eq. (A20)], values are highest in eastern CONUS, where Fig. 4a shows maximal regions in Texas and Oklahoma and a decreasing northward trend away from the Gulf of Mexico. For $\partial E_{\text{pan}}/\partial q$, a function of four drivers [Eq. (A18)], values are highest in western CONUS away from the Pacific Northwest (Fig. 4b); in eastern CONUS, it decreases northward to a minimum around Maine (and in the James Bay region of Ontario and Quebec in Canada). For $\partial E_{\text{pan}}/\partial P_{\text{atm}}$, a function of three drivers [Eq. (A16)], values are highest in western CONUS and, while generally lower in eastern CONUS, increases northward (Fig. 4c). The remaining sensitivities—$\partial E_{\text{pan}}/\partial U_{10}$, $\partial E_{\text{pan}}/\partial R_d$, and

$\partial E_{\text{pan}}/\partial L_d$—exhibit less complicated and more intuitively tractable spatial patterns: they are all functions of three or fewer drivers. For $\partial E_{\text{pan}}/\partial U_{10}$ [Eq. (A17)], values are greatest in the desert Southwest and areas where the vapor pressure deficit (i.e., $e_{\text{sat}} - e_a$) is the greatest (Fig. 4d). Although this is not shown, the converse is also true: the sensitivity of E_{pan} to vapor pressure deficit is greatest in the windiest (mountainous) areas: the Rocky Mountains, the Cascades, the Sierra Nevada, and the Appalachians. This pattern is to be expected from Eq. (1), from which Eq. (A17) is derived. The spatial patterns of $\partial E_{\text{pan}}/\partial R_d$ [Eq. (A19)] and $\partial E_{\text{pan}}/\partial L_d$ [Eq. (A15)] are very similar: both exhibit negative latitudinal and elevational gradients (Figs. 4e,f). Over eastern CONUS, the latitudinal gradient is clearest, with the Appalachians evident as lower sensitivities; in western CONUS, the elevational gradient is clearest, with lower sensitivities picking out the highest elevations of the Rocky Mountains and the Cascade and Sierra Nevada ranges. In this sense, both spatial patterns closely resemble that of mean annual T, which, in the case of $\partial E_{\text{pan}}/\partial L_d$, is its only driver.

Recalling that all variances σ_X^2 and covariances $\sigma_{X,Y}$ are quantified through time series analyses, we can now decompose the overall variability in the output $\sigma_{E_{\text{pan}}}^2$ (Fig. 2) into the variabilities of all of its drivers.

Figure 5 shows the spatial patterns of variability of each driver displayed as its coefficient of variation ($\text{CV}_X = \sigma_X/\mu_X$). The CV_X indicates the potential impact that driver X can have on E_{pan} variability, given that E_{pan} is sensitive to it, and CV_X normalizes this variation across variables of greatly different absolute values. First, from examining the CONUS-wide spatial statistics (i.e., spatial means and standard deviations) of each CV_X, it is apparent that the drivers exhibiting the greatest variability across CONUS are, in descending order, q, U_{10}, R_d, and L_d; T and P_{atm} are the least variable. We next describe each spatial pattern in turn (given the wide variation in CV_X values between the drivers, it was not useful to plot them on a standardized scale; instead, we indicate the range and mean in the text). The pattern of T exhibits the greatest variability in the continental interior (Fig. 5a; northern CONUS and southern Canada) and minima along the coasts—particularly the West Coast [$\min(\text{CV}_T) = 0.0006$, $\text{mean}(\text{CV}_T) = 0.0028$, $\max(\text{CV}_T) = 0.0077$]. The variability of q (Fig. 5b) is greatest in the southwestern CONUS and lowest in eastern CONUS, reaching regional minima along all coasts, and a nationwide minima along the Gulf Coast [$\min(\text{CV}_q) = 0.0141$, $\text{mean}(\text{CV}_q) = 0.0526$, $\max(\text{CV}_q) = 0.1243$]. The pattern of P_{atm} is most variable in the Pacific Northwest and along the mid-Atlantic coast (Fig. 5c), but exhibits regional minima in the continental interior and the desert Southwest [$\min(\text{CV}_{P_{\text{atm}}}) = 0.0003$,
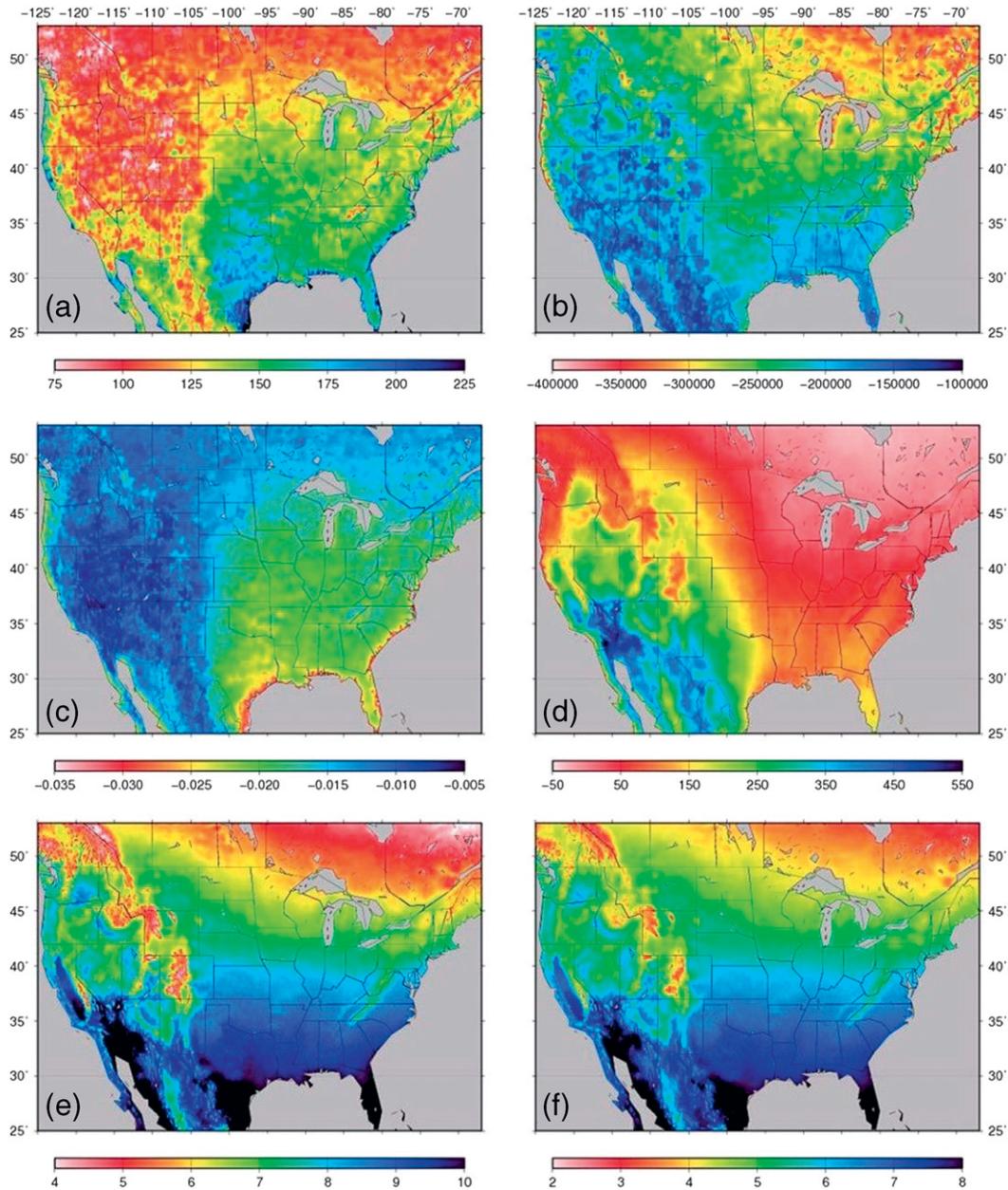
FIG. 4. Sensitivity of annual E_{pan} to the six NLDAS drivers from Eqs. (A15)–(A20), determined using mean values for annual data for 1980–2009: (a) $\partial E_{pan}/\partial T$ [(mm yr^{-1}) K^{-1}], (b) $\partial E_{pan}/\partial q$ [(mm yr^{-1}) (kg kg^{-1})$^{-1}$], (c) $\partial E_{pan}/\partial P_{atm}$ [(mm yr^{-1}) Pa^{-1}], (d) $\partial E_{pan}/\partial U_{10}$ [(mm yr^{-1}) (m s^{-1})$^{-1}$], (e) $\partial E_{pan}/\partial R_d$ [(mm yr^{-1}) (W m^{-2})$^{-1}$], and (f) $\partial E_{pan}/\partial L_d$ [(mm yr^{-1}) (W m^{-2})$^{-1}$]. Note, scales are selected to optimize display of spatial variability and do not represent the complete range of annual sensitivity.

mean($CV_{P_{atm}}$) = 0.0006, max($CV_{P_{atm}}$) = 0.0011]. The variability of U_{10} (Fig. 5d) exhibits a complex spatial pattern, with maxima in the region of the lower Mississippi valley and Texas Gulf Coast, the Colorado River basin, and the interior Pacific Northwest, and minima in much of rest of western CONUS, the Great Plains, and the Northeast [min($CV_{U_{10}}$) = 0.0191, mean($CV_{U_{10}}$) = 0.0392,

max($CV_{U_{10}}$) = 0.1540]. The variability of R_d (Fig. 5e) divides the country into two: a maximum across the eastern half of CONUS and a minimum across the western half [min(CV_{R_d}) = 0.0052, mean(CV_{R_d}) = 0.0231, max(CV_{R_d}) = 0.0519]. The variability of L_d (Fig. 5f) exhibits minima through the center of CONUS, the Great Plains, and in the Northeast, and a maximal region in the
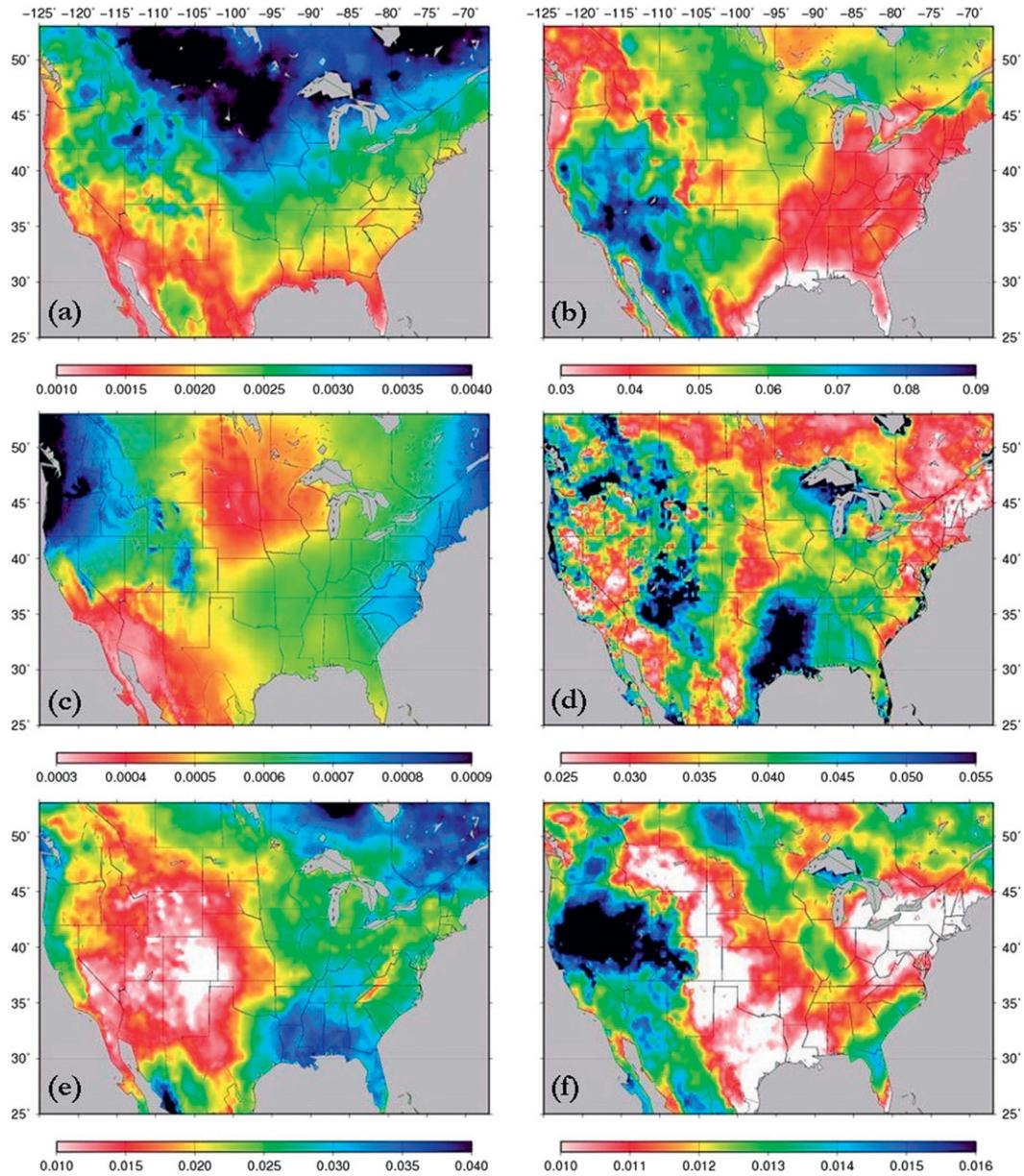
FIG. 5. Coefficients of variation (CV_X) of annual time series of the following six NLDAS drivers, as observed for 1980–2009: (a) T, (b) q, (c) P_{atm}, (d) U_{10}, (e) R_d, and (f) L_d. Note that scales are selected to optimize display of spatial variability and do not represent the complete range of annual CV_X.

western United States, particularly in the Upper Colorado River basin and northern Great Basin [$\min(CV_{L_d}) = 0.0058$, $\text{mean}(CV_{L_d}) = 0.0122$, $\max(CV_{L_d}) = 0.0232$].

Figure 6 shows examples of the spatial patterns of annual and seasonal covariance of T and R_d. The spatial and temporal distribution of positive and negative covariances between T and R_d is notable as it can refute or support the common assumption that T and R_d covary positively and therefore that T can replicate the variability of R_d, as daytime heating of the surface is presumed to follow from clearer skies, and daytime cooling from increased cloud cover. This assumption—referred to as "the T-R_d assumption"—lies at the heart of parameterizations of E_0 that are based solely on T, such as the Thornthwaite (1948) and Hargreaves and Samani (1985) formulations. Clearly, the T-R_d assumption does not hold in regions or seasons that exhibit negative covariance in T and R_d. Figure 6a indicates that the annual T-R_d covariance is indeed positive across the vast majority of CONUS, but not in Florida, the south
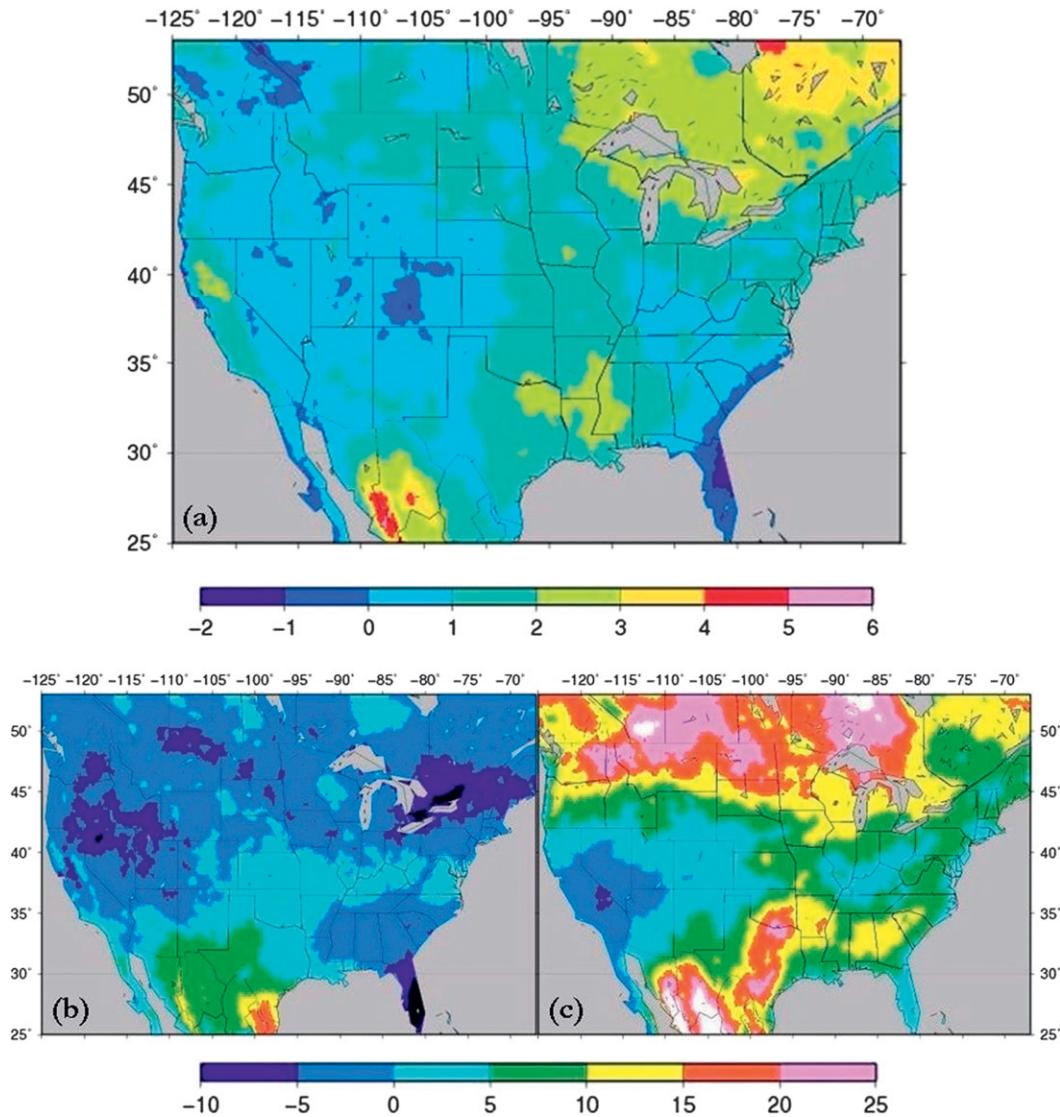
FIG. 6. Covariances of T with R_d [σ_{T,R_d} (K W m^{-2})], as observed from NLDAS data for 1980–2009, for the (a) annual time scale and the months of (b) January and (c) July. Maps (b) and (c) are plotted to the common scale.

Atlantic and Pacific coasts, and in patches of the mountain west. There is also significant seasonal variation in T-R_d covariance. In winter (see Fig. 6b) over much of CONUS—particularly in the northern, western, and southeastern states—heating correlates with cloud cover, presumably as the increased L_d during the day and particularly at night counteracts the cooling effects of decreased daytime R_d, in contravention of the T-R_d assumption. In summer (see Fig. 6c), T and R_d positively covary across all of CONUS except the desert Southwest and patches of Colorado, where they are again negatively correlated. In particular, the T-R_d assumption does not hold in the southeastern CONUS—a region of the highest variability of R_d (Fig. 5e). Here, the

potential errors thrown up by use of parameterizations that rely on the T-R_d assumption will be compounded by the inability to capture the enhanced variability of R_d. In contrast to the covariance of T and R_d, covariances between many of the pairs of drivers can be slight and it may be difficult to draw meaningful conclusions from them.

f. Quantifying variability contributions

As shown in Eq. (7), the contribution to the variability in E_{pan} of any single driver X is a function of terms comprising contributions due to its own variability σ_X^2 and to the variability arising from its covariance with other drivers (Y). The variance terms [i.e., the first term in each line of Eq. (7)] are always positive and so always act

to augment E_{pan} variability; the covariances between drivers and sensitivities [i.e., the components of the remaining terms in each line of Eq. (7)] are often negative and so act to decrease E_{pan} variability. This complicates the issue of comparing the relative contributions of each driver. Recall that in Eq. (7) we defined B_X, the contribution to overall E_{pan} variability of driver X, as the magnitude of the sum of augmenting and reducing terms. We now define the power or strength of driver X (β_X) by normalizing its contribution by the sum of magnitudes of the contributions for all drivers, as follows:

$$\beta_X \equiv \frac{|B_X|}{\sum\limits_{x=1}^{n} |B_X|} \times 100\%. \qquad (10)$$

Note that, because of our use of the magnitudes (the absolute values) of variability in drivers,

$$\sigma^2_{E_{pan}} \neq \sum_{x=1}^{n} |B_X|; \qquad (11)$$

that is, the sum of the variability contributions of the drivers does not necessarily sum to the variance in E_{pan}.

3. Results

Given the multiple steps and inputs to this variability analysis of E_0, there are more ways to parse the results than space here allows. The variety of possible analyses largely depends on the region and season of interest and on the motivation of the analyst. Here, we summarize the main points across CONUS, always focusing on addressing the motivating question raised in the introductory section, "What drives the variability of E_0?".

Figure 7 demonstrates the spatial distribution of each driver's power β_X. Immediately clear here is the dominance of T and, to a lesser degree, q and R_d. The power β_T reaches a maximum of nearly 90% in North Dakota and Minnesota (Fig. 7a), and generally remains over 50% over the northern half of CONUS and the Atlantic coast; it decreases toward the south (particularly southern Florida) and toward the Pacific and Gulf coasts. The distribution of β_{R_d} (Fig. 7e) increases toward the southeastern states and the Pacific coast [max(β_{R_d}) = 73% along the Gulf Coast of Florida], but shows that R_d has the least effect (lowest β_{R_d}) in central CONUS, the interior west, and the Northeast states. The influences of q and U_{10} on the variability of annual E_{pan} (Figs. 7b,d) show extensive regional maxima across the southwestern quadrant of CONUS (where $\beta_{U_{10}}$ reaches ~35% across the Colorado Plateau and β_q reaches ~46% in southern Arizona), but reach their highest values in a small region

of southern Florida [max($\beta_{U_{10}}$) = 45%; max(β_q) = 56%]. The relative weakness of P_{atm} and L_d in affecting the variability of annual E_{pan} is also evident (Figs. 7c,f): nowhere does $\beta_{P_{atm}}$ exceed 2.2%, and only across southeastern Arizona and scattered patches of the western CONUS (<1.5% of CONUS) does β_{L_d}.

By mapping and summarizing annual and monthly β_X, Fig. 8 demonstrates significant time–space variation in which driver contributes the greatest variability to E_{pan}. Figure 9 demonstrates, for each of the six drivers, the spatial pattern of its rank in contributing to annual E_{pan} variability: that is, Fig. 9 decomposes the information regarding annual E_{pan} variability in Fig. 8.

Figure 8a exposes regional climatic distinctions in the dominant drivers of annual E_{pan} variability—that is, those ranked highest. Over 99.95% of CONUS, one of only three individual drivers (T, q, and R_d) is the single dominant driver of annual variability, with β_T ranked first (i.e., highest) across the vast majority of CONUS (92.19% of CONUS by area). The exceptions to this β_T dominance are as follows: northern Texas and the low deserts of California and Arizona (along with much of western Mexico), where β_q is ranked first (4.85% of CONUS); Florida and the northern Gulf Coast, where β_{R_d} is ranked first (2.92% of CONUS); and a few isolated pixels in the desert Southwest and southern Florida, where $\beta_{U_{10}}$ is ranked first (0.05% of CONUS). Figure 9 examines the ranks of each annual variability driver more closely, and indicates that β_T is at its lowest rank (second and third) in Florida, southern Arizona, and California (Fig. 9a). Of further interest is the almost inverse relationship between second ranked drivers: β_q is second across the western two-thirds of CONUS, excluding the Pacific Northwest (Fig. 9b), while β_{R_d} is second or third across the remaining one-third of CONUS, including the Pacific Northwest (Fig. 9e). This relationship generally mimics the distinction between energy- and water-limited hydroclimates across CONUS. The variable $\beta_{U_{10}}$ exhibits a regional maximum in the southern High Plains and Colorado Plateau (Fig. 9d), where it rises to second in rank (first in a few isolated pixels); β_{L_d} is ranked at its highest in northeastern CONUS, the mid-Atlantic coast, and scattered regions of the Pacific Northwest (Fig. 9f), where one would expect regional maxima in the L_d flux; and $\beta_{P_{atm}}$ ranks no higher than fourth (Fig. 9c), with no notable regional patterns.

The summary by area in Fig. 8b and the selected monthly maps in Figs. 8c–f demonstrate the spatiotemporal volatility of the dominant drivers: β_T, β_q, β_{R_d}, and $\beta_{U_{10}}$ clearly ebb and flow across large portions of CONUS, particularly its southern reaches during the warm season. During the summer, R_d dominates over most of the southeastern CONUS (Figs. 8d,e), while U_{10} dominates across the Colorado Plateau and Great Basin
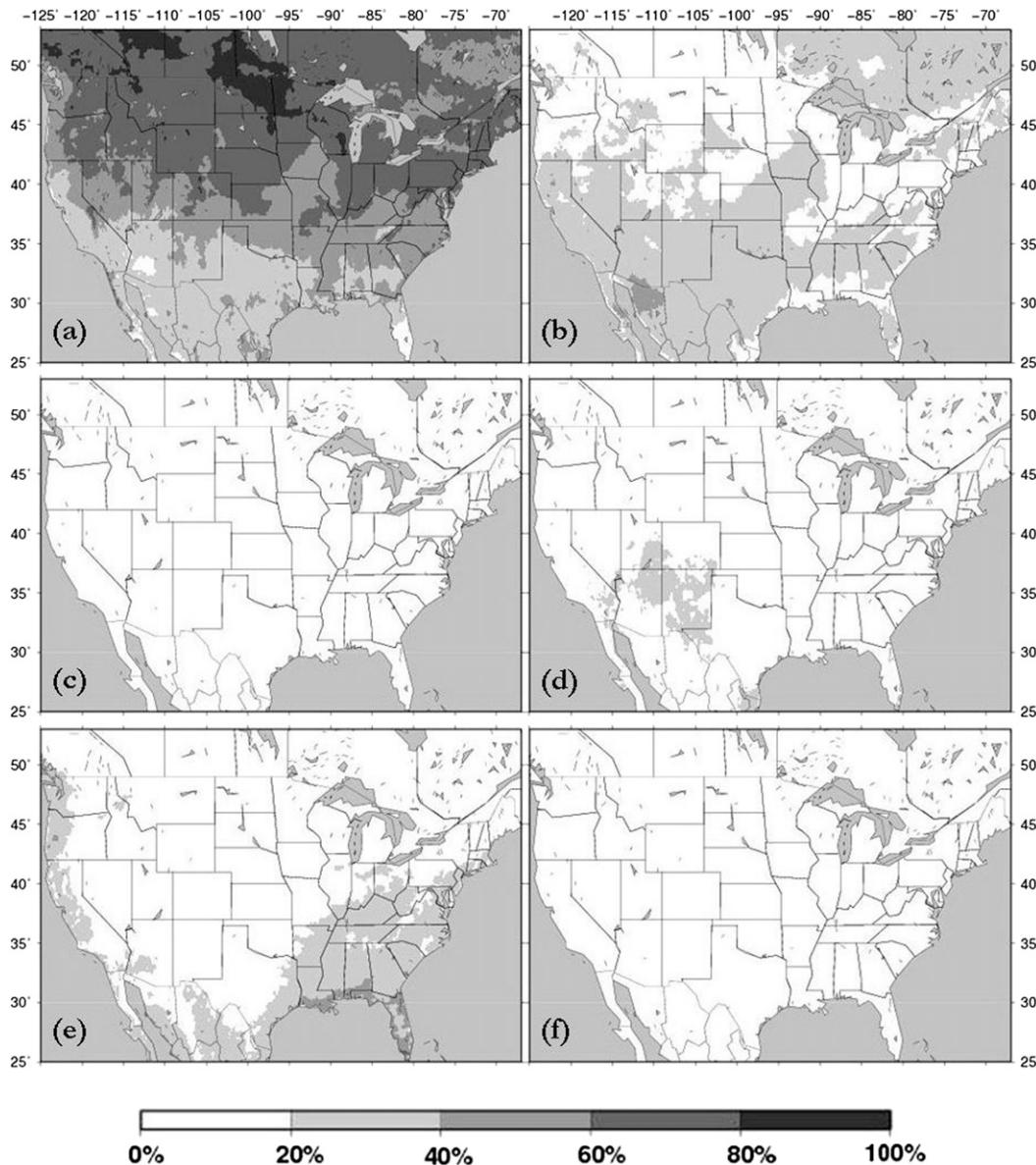
FIG. 7. The power β_X of each of the drivers (a) T, (b) q, (c) P_{atm}, (d) U_{10}, (e) R_d, and (f) L_d in determining annual E_{pan} variability, expressed as percentages of $\sum_{x=1}^{n}|B_X|$ (where X represents the driver).

of southwestern CONUS (Fig. 8e) as a $\beta_{U_{10}}$ maximum emerges in west Texas in May, spreads north and west across the Colorado Plateau and Great Basin, before disappearing after September. Later, in October, q dominates across much of central southern CONUS, as a maximal region of β_q extends from Tennessee to Arizona (Fig. 8f). The evolutions of these seasonal blooms of β_q, β_{R_d}, and $\beta_{U_{10}}$ are indicated in Fig. 8b.

Figure 10 summarizes the relative power β_X of each of the six drivers as it is distributed by area across CONUS. Each curve represents the nonexceedance of β_X with accumulating area. Higher curves indicate drivers that

make more powerful contributions to annual E_{pan} variability (i.e., a greater area of CONUS at a given contribution, or a greater contribution over a given area of CONUS). The minimum and maximum of each curve indicate the range of each β_X, and its shape reflects how β_X varies (the rapid increases in slope of some of the drivers near 0% and 100% of CONUS area are due to the lower and upper tails of the β_X distribution in space). For example, β_{L_d} varies from a minimum of zero (i.e., L_d makes no contribution to the variability in annual E_{pan} over some parts of CONUS) to a maximum of 15.0% (i.e., L_d accounts for 15.0% of the variability in annual E_{pan}).
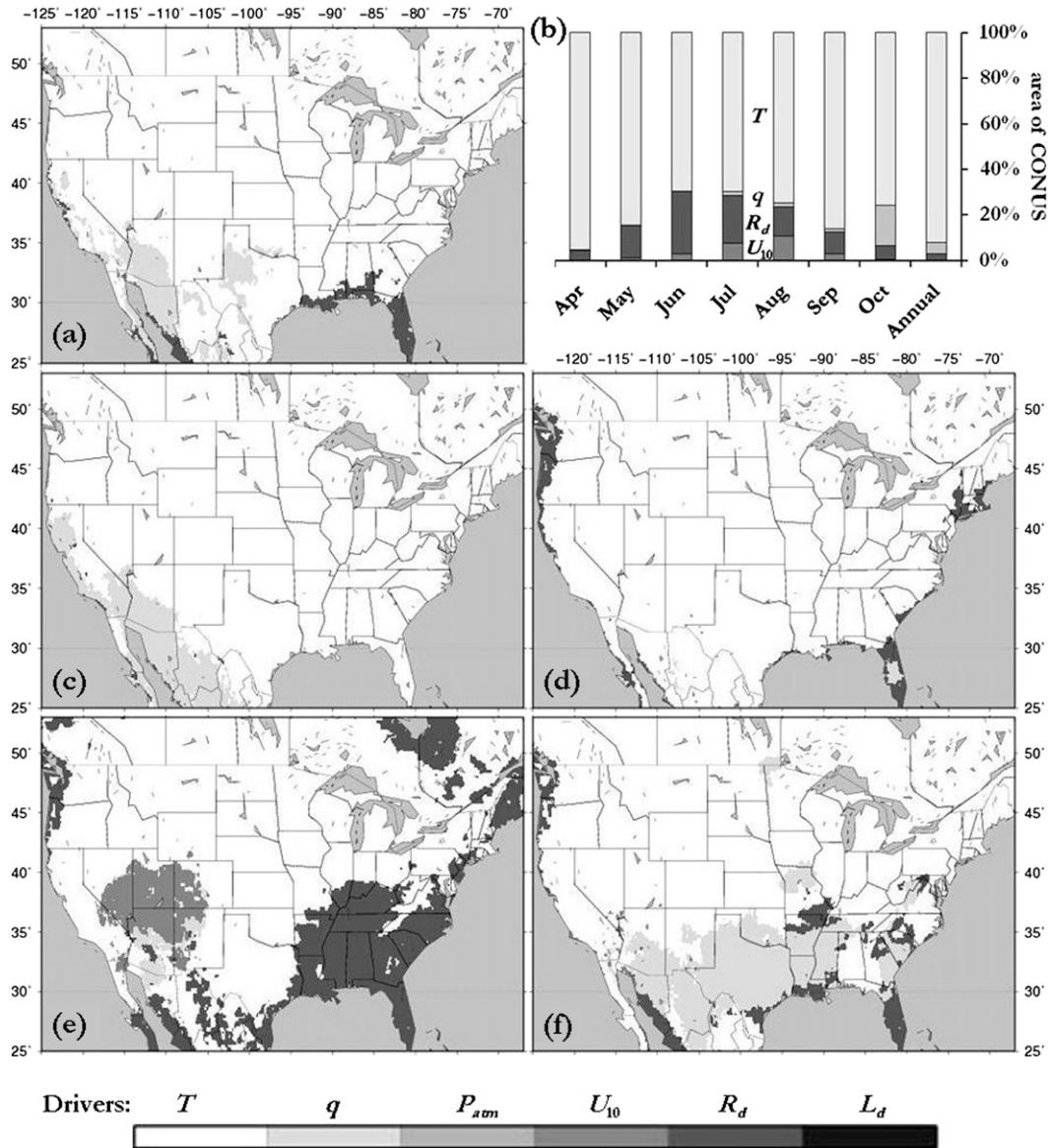
FIG. 8. The dominant drivers of variability in E_{pan} (a),(c)–(f) mapped and (b) summarized across annual and selected monthly time scales. Maps are for (a) annual, (c) January, (d) April, (e) July, and (f) October. Bar graph (b) indicates the areal proportion of CONUS over which each driver dominates at the annual time scale and for selected warm-season months (L_d and P_{atm} are not shown as they do not exhibit dominance at any tested time or space scales). Regions in maps and bars in graph are shaded according to dominant driver.

This summary of the spatial variability of annual β_X indicates the relative significance of drivers in space and time. That the power curve for T is the highest indicates that, overall, it is the most powerful driver of annual E_{pan} variability across CONUS. Indeed, for 50% of CONUS, T contributes at least 58.3% of annual E_{pan} variability. The next two most-powerful drivers are, in order, q and R_d. In fact, q is ranked as second or first driver across 67% of CONUS, while R_d is ranked second or first driver across 31% of CONUS. Next, U_{10} ranks

first or second over only 2.5% of CONUS for annual E_{pan} variability. However, its contribution to seasonal E_{pan} variability is important: the region of U_{10} significance that emerges in the summer months (see Fig. 8e) corresponding to the uptick in the slope of the U_{10} power curve accounts for ~30% of CONUS (i.e., above ~70% of CONUS on the x axis). Clearly P_{atm} and, to a lesser degree, L_d are the least significant drivers of annual E_{pan} variability. This observation is supported by Figs. 7–9, which show that P_{atm} and L_d generally contribute little
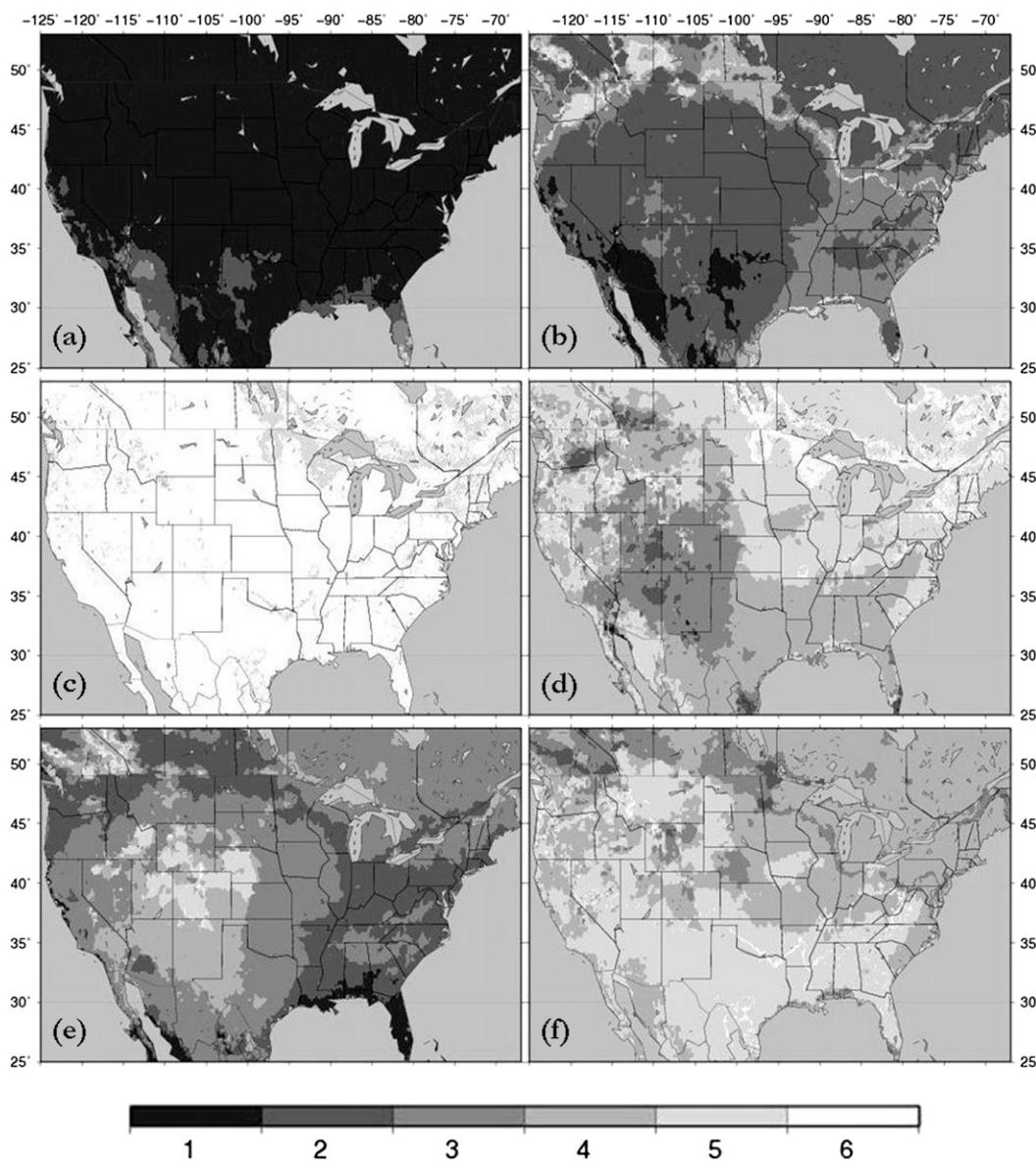
FIG. 9. Rank of power β_X of each driver (a) T, (b) q, (c) P_{atm}, (d) U_{10}, (e) R_d, and (f) L_d of annual E_{pan} variability (where X represents the driver).

to the variability in annual E_{pan} (Fig. 7), that neither is anywhere the most significant contributor to either annual or monthly E_{pan} variability (Fig. 8), and that β_{L_d} and $\beta_{P_{atm}}$ peak at ranks of 2 and 3, respectively (Fig. 9).

4. Summary and conclusions

Toward improving our understanding of the variation of E_0 (and hence ET) in space and time, and consequently our ability to monitor and predict CONUS-wide energy and water cycles, this first-order, second-moment variability analysis of a physically sound measure of

atmospheric evaporative demand demonstrates the contributions to temporal and spatial variability of annual E_0 by all of its drivers. We have outlined the methodology and examined a measure of the power of each driver as its relative magnitudes of variability normalized by the sum of magnitudes from all drivers. This power analysis quantifies the spatial and temporal volatility of the importance of these variability drivers, indicating where each driver dominates and in which season. Like other work (Rotstayn et al. 2006; Roderick et al. 2007), we show that our central assumption—that E_{pan} from the PenPan model synthesizes E_0 well—holds
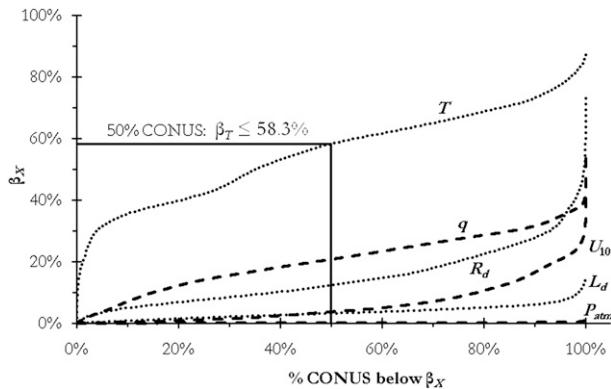
FIG. 10. The power-area response curves for each driver across CONUS. The y axis indicates β_X, which is the percentage contribution of each driver (X) to the total variability of annual E_{pan} from Eq. (10). The x axis indicates the CONUS area percentage across which this value of β_X is not exceeded.

up well against E_{pan} observations. Although specific findings [e.g., the sensitivity expressions in Eqs. (A15)–(A20) for our particular suite of six drivers] relate only to the PenPan model, the primary conclusions apply across the gamut of physically based combination equations of E_0. This analysis is part of a broader effort to provide a long-term reanalysis of physically based and accurate NLDAS-driven E_0 across CONUS, from 1979 to within a few days of the present.

Numerous parameterizations currently exist for E_0, ranging from models favoring parameter parsimony and based solely on T to more physically representative formulations including radiative and advective dynamics. Correctly identifying and including the dominant drivers of E_0 variability is crucial for any hydrologic application that estimates actual ET from LSMs driven by E_0, such as streamflow forecasting and drought analyses (e.g., Hobbins et al. 2008). The results presented herein have broad implications and potential utility across hydrology, as they allow for the identification of the drivers that require the most attention and possibly correction in such formulations, versus those that may be omitted in moving to a forecast context where fewer data streams may be available to drive a model. For modelers motivated by parameter parsimony, this analysis indicates that one could eliminate the least-powerful driver, P_{atm}, from the parameterization of E_{pan}: instead, its spatial variability may be captured by surface elevation and consideration of the atmosphere in purely hydrostatic balance. Further parsimony gains might be made from parameterizing the second least-powerful driver, L_d, by e_a, T, and R_d (e.g., Shuttleworth 1992). In the context of forecasting E_0 at river forecast centers (RFCs)—as distinct from the

reanalyses examined in this paper—estimates of effective cloud amount, T, dewpoint temperature, and U_2 from numerical weather prediction (NWP) models are used to predict E_0; these variables represent the four most-powerful drivers used in our analysis (R_d, T, q, and U_{10}, respectively). The influence of R_d on the variability in E_0 underscores the paramount importance of parameterizing R_d accurately from effective cloud amount. Of course, the estimation of T and—depending on region and season—q in forecasting E_0 is of prime importance, but it is generally assumed that NWP-based techniques (and climate models) already forecast or predict these drivers effectively.

Because of their simplicity, E_0 parameterizations based solely on T (e.g., Thornthwaite 1948; Hamon 1961; Hargreaves and Samani 1985) are used in areas and applications for which they are ill suited—for example, the use of the PDSI in drought monitoring and the consequent flawed observations of midlatitude drying (Alley et al. 2007). As we show here, across distinct regions of CONUS, T is not the greatest driver of annual E_0 variability (across 10% of CONUS, or 8×10^5 km^2, T provides less than 36% of the variability of E_0, while across more than half of CONUS, using T alone limits one to less than 42% of the observed variability in E_0). In many regions where T does dominate annual E_0 variability, during the important months of the growing season this dominance waxes and wanes inversely with that of q and R_d, with U_2 further complicating the picture.

The seasonal and regional weaknesses of T-based parameterizations arise because T cannot be used to capture the variability of R_d in E_0 parameterizations. This finding follows from, first, the differences in sensitivity of E_0 to T and R_d and in their variabilities, and second, the negative correlation of T and R_d over much of CONUS on an annual time scale and over nearly all of CONUS for some months. In many of these regions—particularly southeastern CONUS—R_d is the top-ranked variability driver, underscoring the importance of its direct modeling (as opposed to substitution by the questionable T-R_d assumption). We find that T-based parameterizations of E_0 cannot capture its intra-annual variability, which complements earlier findings (Hobbins et al. 2008; Donohue et al. 2010) that such parameterizations do not work at interannual time scales. We therefore conclude that T-based parameterizations of E_0 are to be avoided at all time scales. We have shown that at an annual (and monthly) basis, across CONUS, parameterizations should include, at the least, R_d, T, q, and U_{10}. This finding also points to the fact that, depending on the region and goals of analysis, different drivers may dominate: for example, in attributing long-term trends in observed monthly E_{pan} in Australia to the relative effects

trends in drivers of the PenPan model, Roderick et al. (2007) found that U_2 dominates trends.

We have explored and decomposed the variability of annual E_0, yet numerous related questions remain unexplored. Using these data and methodologies, smaller-scale analyses could target seasonal and regional demands, such as the all-important growing season in the western United States, where agriculture and municipalities largely depend on water stored from the spring melt. Specifically for the Colorado Basin RFC, the bloom of high $\beta_{U_{10}}$ in the late spring and summer across the Colorado Plateau and Great Basin implies that replacing a temperature-based model with a combination-type model would improve the monitoring and forecasting of E_0 and, consequently, the region's hydrologic applications such as streamflow forecasting. Overall, we find that regional and seasonal variations in E_0 forcing dynamics are important from a water balance perspective, and argue for the adoption of E_0 estimation approaches that fully represent these variations.

APPENDIX A

Formulation of the PenPan Model and Sensitivities to Its Drivers

a. The PenPan model

The PenPan model (Rotstayn et al. 2006) differs from its parent Penman (1948) model by accounting for the effects on the radiation incident to the pan sides (an increase in net irradiance) and the presence of bird guards (a reduction), as well as the effects on vapor transfer of extra turbulence as wind crosses the pan sides. Herein we summarize the aspects of the formulation of the PenPan model that pertain to its expression in Eq. (A14), and the sensitivities of E_{pan} to its drivers [Eqs. (A15)–(A20)] derived from Eq. (14). More detail of the model is given in Rotstayn et al. (2006). Here, we address first the energetic component, then the advective.

The energetic input to the pan, or the net available energy, is expressed as

$$Q_n = R_n + L_n + \frac{\partial W}{\partial t}, \tag{A1}$$

where R_n is the net shortwave radiation (W m^{-2}), L_n is the net longwave radiation (W m^{-2}), and $\partial W/\partial t$ is the time rate of change of heat energy stored in the pan (W m^{-2}). Following, we deal with each term in turn.

The PenPan shortwave parameterization formulates the total shortwave radiation incident to the pan $R_{d,P}$ as the observed shortwave incident to the ground surface R_d multiplied by the summation of three terms. These terms account for an increase in shortwave radiation due to the interception of direct beam radiation, the interception of diffuse radiation, and the interception of extra shortwave radiation reflected from the ground surface to the pan sides, as follows:

$$R_{d,P} = R_d[f_{dir}P_{rad} + 1.42(1 - f_{dir}) + 0.42\alpha_S]. \tag{A2}$$

In Eq. (A2), all parenthetical parameters are dimensionless: f_{dir} is the fraction of R_d that is direct beam radiation and this fraction is itself factored by the pan radiation factor P_{rad} to account for the extra shortwave radiation intercepted by the pan sides. The surface albedo α_S is set to 0.22, a typical value for short green grass. Here f_{dir} is given by

$$f_{dir} = -0.11 + 1.31\frac{R_d}{R_{toa}}, \tag{A3}$$

while the pan radiation factor P_{rad} varies as the following function of latitude φ (rad; positive north of the equator):

$$P_{rad} = 1.32 + 4 \times 10^{-4}\left(\frac{180\phi}{\pi}\right) + 8 \times 10^{-5}\left(\frac{180\phi}{\pi}\right)^2. \tag{A4}$$

In Eq. (A3), the extraterrestrial or top-of-atmosphere shortwave radiation R_{toa} (W m^{-2}) is calculated following Shuttleworth (1992):

$$R_{toa} = 15.392\frac{\lambda}{86\,400}d_r(\omega_s \sin\phi \sin\delta + \cos\phi \cos\delta \sin\omega_s), \tag{A5}$$

where the constant 15.392 represents the solar constant expressed as an evaporative equivalent (mm day^{-1}), and λ is the latent heat of vaporization [J kg^{-1}; from Eq. (A13) below]. The other variables are time dependent—d_r is the (dimensionless) relative distance from the earth to

the sun, δ is the solar declination (rad), and ω_s is the sunset hour angle (rad)—and expressions for them are available in Allen et al. (1998).

The net shortwave radiation to the pan R_n is then calculated from

$$R_n = (1 - \alpha_P)R_{d,P}, \tag{A6}$$

setting α_P to 0.14, for the albedo of a U.S. class-A pan (Rotstayn et al. 2006).

Formulation of the net longwave radiation L_n to the pan proceeds by assuming that the water surface emits longwave radiation as a blackbody and ignoring longwave radiation from the pan sides, thereby yielding an overall bulk emissivity ε of 1 (Rotstayn et al. 2006). Net longwave radiation L_n to the pan is therefore given by Eq. (A7) below [note that in the original PenPan formulation, Linacre (1994) assumed an annual mean L_n of -40 W m^{-2}]:

$$L_n = L_d - \varepsilon\sigma T^4. \tag{A7}$$

Following guidelines in Roderick et al. (2009a), the monthly time scale in this analysis justifies the steady-state assumption and permits assumption of negligible heat-storage changes in the pan water $\partial W/\partial t$. Equation (A1) for the available energy for evaporation Q_n then becomes

$$Q_n = R_n + L_n. \tag{A8}$$

Turning to the advective component of the E_{pan} formulation, the vapor transfer function (or "wind function") $f_q(U_2)$ (kg m^{-2} s^{-1} Pa^{-1}) is a linear expression, similar to that first derived by Penman (1948):

$$f_q(U_2) = 1.39 \times 10^{-8}(1 + 1.35U_2), \tag{A9}$$

where U_2 is in m s^{-1}.

To account for the extra surface area (i.e., the sides and bottom of the pan) available for sensible heat transfer over that available for vapor transfer, γ is everywhere multiplied by the dimensionless ratio of effective surface areas for the transfers of heat and water-vapor a_P:

$$a_P = \frac{f_h(U_2)}{f_q(U_2)} = 2.4. \tag{A10}$$

The saturated vapor pressure e_{sat} (Pa) derives from the following relation:

$$e_{\text{sat}} = 610.8\exp\left[\frac{17.27(T - 273.15)}{237.3 + (T - 273.15)}\right], \tag{A11}$$

for T given in units of K. The actual vapor pressure e_a (Pa) derives from the following relation:

$$e_a = \frac{qP_{\text{atm}}}{0.622 + 0.378q}, \tag{A12}$$

for dimensionless q and P_{atm} in units of Pa.

Finally, the latent heat of vaporization λ (J kg^{-1}) is given as the following function of T (K):

$$\lambda = 2.501 \times 10^6 - 2361(T - 273.15). \tag{A13}$$

To simplify the derivation of the sensitivities of E_{pan} to its drivers (particularly to T), we approximate the functions of $\Delta/(\Delta + a_p\gamma)$ and $a_p\gamma/(\Delta + a_p\gamma)$ in a similar fashion to Brutsaert (2005), using the linear function of T shown in Eqs. (B1)–(B3) (see appendix B). Then, into Eq. (1), we further substitute Eqs. (A2), (A3), and (A5) to (A8) for Q_n, Eqs. (2) and (A9) for $f_q(U_2)$, Eq. (A11) for e_{sat}, Eq. (A12) for e_a, and Eq. (A13) for λ. This reveals the following complete expression for E_{pan} (kg m^{-2} s^{-1}) from the PenPan model of synthetic E_{pan} in terms of its six drivers (R_d, L_d, T, U_{10}, q, and P_{atm}), constants (ε, σ, α_P, and α_S,), and parameters that are known with certainty for a given point in time (d_r, φ, δ), space (P_{rad}), or both (R_{toa}, ω_s):

$$
\begin{aligned}
E_{\text{pan}} = {}& \frac{0.0115(T - 273.15) + 0.2006}{2.501 \times 10^6 - 2361(T - 273.15)} \\
& \times \left\{(1 - \alpha_P)R_d\left[R_d\frac{1.31}{R_{\text{toa}}}(P_{\text{rad}} - 1.42) - 0.11P_{\text{rad}} + 0.42\alpha_S + 1.42 \times 1.11\right] + L_d - \varepsilon\sigma T^4\right\} \\
& + [0.7994 - 0.0115(T - 273.15)]1.39 \times 10^{-8}\left[1 + 1.35U_{10}\left(\frac{2}{10}\right)^{1/7}\right] \\
& \times \left\{610.8\exp\left[\frac{17.27(T - 273.15)}{237.3 + (T - 273.15)}\right] - \frac{qP_{\text{atm}}}{0.622 + 0.378q}\right\}.
\end{aligned}
\tag{A14}
$$

b. Sensitivities of PenPan-derived E_{pan} to the model drivers

Equation (A14) then allows for expressions for the sensitivity of E_{pan} to each of its drivers to be derived by partial differentiation with respect to the driver. Following, in Eqs. (A15)–(A20), these expressions are shown in order of increasing complexity. The sensitivity of E_{pan} to L_d is as follows:

$$\frac{\partial E_{\mathrm{pan}}}{\partial L_d} = \frac{f_T}{\lambda}. \quad (A15)$$

The sensitivity of E_{pan} to P_{atm} is as follows:

$$\frac{\partial E_{\mathrm{pan}}}{\partial P_{\mathrm{atm}}} = \frac{(f_T - 1)f_q(U_2)q}{0.622 + 0.378q}. \quad (A16)$$

The sensitivity of E_{pan} to U_{10} is as follows:

$$\frac{\partial E_{\mathrm{pan}}}{\partial U_{10}} = (1 - f_T)1.39 \times 10^{-8} \times 1.35 \left(\frac{2}{10}\right)^{1/7} (e_{\mathrm{sat}} - e_a). \quad (A17)$$

The sensitivity of E_{pan} to q is as follows:

$$\frac{\partial E_{\mathrm{pan}}}{\partial q} = (f_T - 1)f_q(U_2)P_{\mathrm{atm}}\frac{0.622}{(0.622 + 0.378q)^2}. \quad (A18)$$
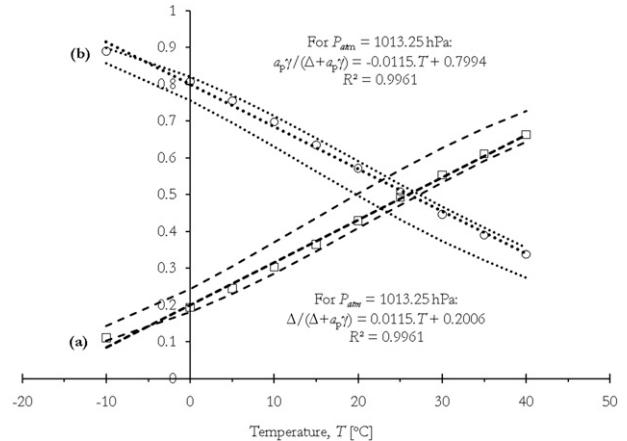

FIG. B1. Approximations of $\Delta/(\Delta + a_p\gamma)$ [squares and bold dashed line marked (a)] and $a_p\gamma/(\Delta + a_p\gamma)$ [circles and bold dotted line marked (b)] by a linear f_T for $P_{\mathrm{atm}} = 1013.25$ hPa. The dashed lines represent analytic $\Delta/(\Delta + a_p\gamma)$ and $a_p\gamma/(\Delta + a_p\gamma)$ at $P_{\mathrm{atm}} = 750$ hPa [upper (a), lower (b)], and 1100 hPa [lower (a), upper (b)].

The sensitivity of E_{pan} to R_d is as follows:

$$\frac{\partial E_{\mathrm{pan}}}{\partial R_d} = \frac{f_T(1 - \alpha_P)}{\lambda}\left[R_d\frac{2.62}{R_{\mathrm{toa}}}(P_{\mathrm{rad}} - 1.42) - 0.11P_{\mathrm{rad}} + 0.42\alpha_S + 1.5762\right]. \quad (A19)$$

The sensitivity of E_{pan} to T is as follows:

$$\frac{\partial E_{\mathrm{pan}}}{\partial T} = \frac{f_T}{\lambda}4\varepsilon\sigma T^3 + (R_n + L_d - \varepsilon\sigma T^4)\frac{0.0115\lambda + 2361f_T}{\lambda^2}$$
$$+ (1 - f_T)f_q(U_2)e_{\mathrm{sat}}\frac{4098.171}{(T - 35.85)^2} - 0.0115f_q(U_2)(e_{\mathrm{sat}} - e_a). \quad (A20)$$

APPENDIX B

Simplifications

To simplify the derivation of the partial derivative of E_{pan} with respect to T, we approximate the functions of $\Delta/(\Delta + a_p\gamma)$ and $a_p\gamma/(\Delta + a_p\gamma)$ in Eq. (1) as linear functions of T, in a similar fashion to Brutsaert (2005), as follows:

$$\frac{\Delta}{\Delta + a_p\gamma} = g(T, P_{\mathrm{atm}}) \approx f_T = a(T - 273.15) + b, \quad (B1)$$

and, therefore:

$$\frac{a_p\gamma}{\Delta + a_p\gamma} \approx 1 - f_T. \quad (B2)$$

As shown in Fig. B1, for a fixed P_{atm} of 1013.25 hPa (data points shown, linear trends shown as solid lines), analytic values of $\Delta/(\Delta + a_p\gamma)$ and $a_p\gamma/(\Delta + a_p\gamma)$ exhibit a correlation coefficient R^2 of 0.9961 to a linear f_T across a wide range of T ($-10°$ to 40°C). Across the range $P_{\mathrm{atm}} = 750$ to 1013.25 hPa, the slopes of these relationships are insensitive to P_{atm}, varying only 5% from $a = 0.0121$ at $P_{\mathrm{atm}} = 550$ hPa to $a = 0.0115$ at $P_{\mathrm{atm}} = 1013.25$ hPa.

The variable a was then set to a value of 0.0115 (derived for sea level P_{atm}) across the range of P_{atm}. The linear f_T approximation used for $\Delta/(\Delta + a_p\gamma)$ is therefore defined throughout this study as follows:

$$f_T = 0.0115(T - 273.15) + 0.2006, \qquad \text{(B3)}$$

with $a_p\gamma/(\Delta + a_p\gamma)$ approximated by $1 - f_T$.

APPENDIX C

Symbol List

a. NLDAS drivers

q	2-m specific humidity (kg kg^{-1})
L_d	Downwelling longwave radiation (W m^{-2})
P_{atm}	Surface pressure (Pa)
R_d	Downwelling shortwave radiation (W m^{-2})
T	2-m air temperature (K)
U_{10}	10-m wind speed (m s^{-1})

b. Evaporation-related fluxes

E_0	Atmospheric evaporative demand (includes E_{pan}) (mm day^{-1})
E_{pan}	Pan evaporation (mm day^{-1})
ET	Actual evapotranspiration (mm day^{-1})

c. Intermediate variables

α_P	Albedo of a U.S. class-A pan (dimensionless)
α_S	Surface albedo (dimensionless)
β_{X0}	Power or strength of driver X (%)
γ	Psychrometric constant (Pa K^{-1})
$\boldsymbol{\gamma}$	Vector of all partial derivatives
$\boldsymbol{\gamma}^{\mathrm{T}}$	Transpose of $\boldsymbol{\gamma}$
$\partial E_{pan}/\partial X$	Sensitivity of E_{pan} to driver X [mm day^{-1} (units of X)$^{-1}$]
$\partial W/\partial t$	Time rate of change of heat energy stored in the pan (W m^{-2})
δ	Solar declination (rad)
ε	Overall bulk emissivity (dimensionless)
λ	Latent heat of vaporization (J kg^{-1})
φ	Latitude north (rad)
$\sigma_{E_{pan}}^2$	Variance of E_{pan} (mm day^{-1})^2
σ_X^2	Variance of subscripted variable (units of X)^2
σ_{SB}	Stefan–Boltzmann constant (W m^{-2} K^{-4})
σ_X	Standard deviation of driver X (units of X)

$\sigma_{X,Y}$	Covariance of drivers X and Y [(units of X) $\times$ (units of Y)]
μ_X	Mean of driver X (units of X)
ω_s	Sunset hour angle (rad)
Δ	de_{sat}/dT at T (Pa K^{-1})
a	Slope parameter in f_T (1/T)
a_p	Ratio of effective surface areas for the transfers of heat and water vapor (dimensionless)
d_r	Relative distance from the earth to the sun (dimensionless)
e_a	Actual vapor pressure (Pa)
e_{sat}	Saturated vapor pressure (Pa)
f_{dir}	Fraction of R_d that is direct beam radiation (dimensionless)
$f_q(U_2)$	Vapor transfer function (or "wind function") (kg m^{-2} s^{-1} Pa^{-1})
f_T	Linear approximation to $\Delta/(\Delta + a_p\gamma)$ (dimensionless)
m	Number of possible pairs of drivers (dimensionless)
max($\cdot$)	Maximum of ($\cdot$) across CONUS [units of ($\cdot$)]
mean($\cdot$)	Mean of ($\cdot$) across CONUS [units of ($\cdot$)]
min($\cdot$)	Minimum of ($\cdot$) across CONUS [units of ($\cdot$)]
n	Number of drivers (dimensionless)
z_1	Height for which wind speed data are required (m)
z_2	Height at which wind speed data are available (m)
B_X	Magnitude of the sum of augmenting and reducing terms (W m^{-2})^2
$\mathbf{C}$	Covariance matrix of variances σ_X^2 of, and covariances $\sigma_{X,Y}$ between, drivers X and Y
CV$_X$	Coefficient of variation of driver X (dimensionless)
Q_n	Net available energy (W m^{-2})
L_n	Net longwave radiation (W m^{-2})
P_{rad}	Pan radiation factor (dimensionless)
R^2	Correlation coefficient (dimensionless)
$R_{d,P}$	Total shortwave radiation incident to an evaporation pan (W m^{-2})
R_n	Net shortwave radiation (W m^{-2})
R_{toa}	Extraterrestrial or top-of-atmosphere shortwave radiation (W m^{-2})
U_2	2-m wind speed (m s^{-1})
U_z	Wind speed at z (m) above the ground (m s^{-1})
X	Single driver (units of X)
Y	Single driver (units of Y)

REFERENCES

Allen, R. G., L. S. Pereira, D. Raes, and M. Smith, 1998: Crop evapotranspiration: Guidelines for computing crop water requirements. FAO Irrigation and Drainage Paper 56, 300 pp.

Alley, R., and Coauthors, 2007: Summary for policymakers. *Climate Change 2007: The Physical Science Basis,* S. Solomon et al., Eds., Cambridge University Press, 1–18. [Available online at http://www.ipcc.ch/pdf/assessment-report/ar4/wg1/ar4-wg1-spm.pdf.]

Blaney, H. F., and W. D. Criddle, 1950: Determining water requirements in irrigated areas from climatological and irrigation data. U.S. Soil Conservation Service Tech. Paper 96, 48 pp.

Brutsaert, W., 1982: *Evaporation into the Atmosphere: Theory, History, and Applications.* D. Reidel, 299 pp.

——, 2005: *Hydrology: An Introduction.* Cambridge University Press, 605 pp.

——, and M. B. Parlange, 1998: Hydrologic cycle explains the evaporation paradox. *Nature,* **396,** 30.

Chen, D., G. Gao, C.-Y. Xu, J. Guo, and G. Ren, 2005: Comparison of the Thornthwaite method and pan data with the standard Penman-Monteith estimates of reference evapotranspiration in China. *Climate Res.,* **28,** 123–132.

Dai, A., T. Trenberth, and K. E. Qian, 2004: A global dataset of Palmer Drought Severity Index for 1870–2002: Relationship with soil moisture and effects of surface warming. *J. Hydrometeor.,* **5,** 117–130.

Donohue, R. J., T. R. McVicar, and M. L. Roderick, 2010: Assessing the ability of potential evaporation formulations to capture the dynamics in evaporative demand within a changing climate. *J. Hydrol.,* **386,** 186–197, doi:10.1016/j.jhydrol.2010.03.020.

Eslamian, S., M. J. Khordadi, and J. Abedi-Koupai, 2011: Effects of variations in climatic parameters on evapotranspiration in the arid and semi-arid regions. *Global Planet. Change,* **78,** 188–194, doi:10.1016/j.gloplacha.2011.07.001.

Farnsworth, R. K., E. S. Thompson, and E. L. Peck, 1982: Evaporation atlas for the contiguous 48 United States. NOAA Tech. Rep. NWS 33, 27 pp. [Available online at http://www.weather.gov/oh/hdsc/PMP_related_studies/TR33.pdf.]

Hamon, W. R., 1961: Estimating potential evapotranspiration. *J. Hydraul. Div., Amer. Soc. Civ. Eng.,* **87,** 107–120.

Hargreaves, G. H., and Z. A. Samani, 1985: Reference crop evapotranspiration from temperature. *Appl. Eng. Agric.,* **1,** 96–99.

Hobbins, M. T., J. A. Ramírez, and T. C. Brown, 2004: Trends in pan evaporation and actual evapotranspiration across the conterminous U.S.: Paradoxical or complementary? *Geophys. Res. Lett.,* **31,** L13503, doi:10.1029/2004GL019846.

——, A. Dai, M. L. Roderick, and G. D. Farquhar, 2008: Revisiting the parameterization of potential evaporation as a driver of long-term water balance trends. *Geophys. Res. Lett.,* **35,** L12403, doi:10.1029/2008GL033840.

Johnson, F., and A. Sharma, 2010: A comparison of Australian open water body evaporation trends for current and future climates estimated from class A evaporation pans and general circulation models. *J. Hydrometeor.,* **11,** 105–121.

Linacre, E. T., 1994: Estimating U.S. class A pan evaporation from few climate data. *Water Int.,* **19,** 5–14.

Mailhot, A., and J.-P. Villeneuve, 2003: Mean-value second-order uncertainty analysis method: Application to water quality

modelling. *Adv. Water Resour.,* **26,** 491–499, doi:10.1016/S0309-1708(03)00006-X.

Mitchell, K. E., and Coauthors, 2004: The multi-institution North American Land Data Assimilation System (NLDAS): Utilizing multiple GCIP products and partners in a continental distributed hydrological modeling system. *J. Geophys. Res.,* **109,** D07S90, doi:10.1029/2003JD003823.

Moonen, A. C., L. Ercoli, M. Mariotti, and A. Masoni, 2002: Climate change in Italy indicated by agrometeorological indices over 122 years. *Agric. For. Meteor.,* **111,** 13–27.

NCDC, cited 2011a: NCDC TD3200 U.S. cooperative summary of day, 1890(1948)-cont. [Available online at http://rda.ucar.edu/datasets/ds510.0/.]

——, cited 2011b: NCDC TD3220 U.S. cooperative summary of month, 1851(1931)-cont. [Available online at http://rda.ucar.edu/datasets/ds560.0/.]

Ohmura, A., and M. Wild, 2002: Is the hydrological cycle accelerating? *Science,* **298,** 1345–1346.

Palmer, W. C., 1965: Meteorological drought. Office of Climatology, U.S. Weather Bureau, U.S. Department of Commerce Research Paper 45, 58 pp. [Available online at http://lwf.ncdc.noaa.gov/temp-and-precip/drought/docs/palmer.pdf.]

Penman, H. L., 1948: Natural evaporation from open water, bare soil, and grass. *Proc. Roy. Soc. London,* **A193,** 120–145.

Peterson, T. C., V. S. Golubev, and P. Y. Groisman, 1995: Evaporation losing its strength. *Nature,* **377,** 687–688.

Roderick, M. L., and G. D. Farquhar, 2002: The cause of decreased pan evaporation over the past 50 years. *Science,* **298,** 1410–1411.

——, L. D. Rotstayn, G. D. Farquhar, and M. T. Hobbins, 2007: On the attribution of changing pan evaporation. *Geophys. Res. Lett.,* **34,** L17403, doi:10.1029/2007GL031166.

——, M. T. Hobbins, and G. D. Farquhar, 2009a: Pan evaporation trends and the terrestrial water balance. I. Principles and observations. *Geogr. Compass,* **3,** 746–760, doi:10.1111/j.1749-8198.2008.00213.x.

——, ——, and ——, 2009b: Pan evaporation trends and the terrestrial water balance. II. Energy balance and interpretation. *Geogr. Compass,* **3,** 761–780, doi:10.1111/j.1749-8198.2008.00214.x.

Rotstayn, L. D., M. L. Roderick, and G. D. Farquhar, 2006: A simple pan-evaporation model for analysis of climate simulations: Evaluation over Australia. *Geophys. Res. Lett.,* **33,** L17715, doi:10.1029/2006GL027114.

Shuttleworth, W. J., 1992: Evaporation. *Handbook of Hydrology,* D. R. Maidment, Ed., McGraw-Hill, 4.1–4.53.

——, A. Serrat-Capdevila, M. L. Roderick, and R. L. Scott, 2009: On the theory relating changes in area-average and pan evaporation. *Quart. J. Roy. Meteor. Soc.,* **135,** 1230–1247, doi:10.1002/qj.434.

Stanhill, G., 2002: Is the class A evaporation pan still the most practical and accurate meteorological method for determining irrigation water requirements? *Agric. For. Meteor.,* **112,** 233–236.

Svoboda, M., and Coauthors, 2002: The Drought Monitor. *Bull. Amer. Meteor. Soc.,* **83,** 1181–1190.

Thom, A. S., J.-L. Thony, and M. Vauclin, 1981: On the proper employment of evaporation pans and atmometers in estimating potential transpiration. *Quart. J. Roy. Meteor. Soc.,* **107,** 711–736.

Thornthwaite, C. W., 1948: An approach toward a rational classification of climate. *Geogr. Rev.,* **38,** 55–94.